Joule

Article

Origami-structured triboelectric nanogenerator for energy and information co-harvesting from a single hand tap

Graphical abstract

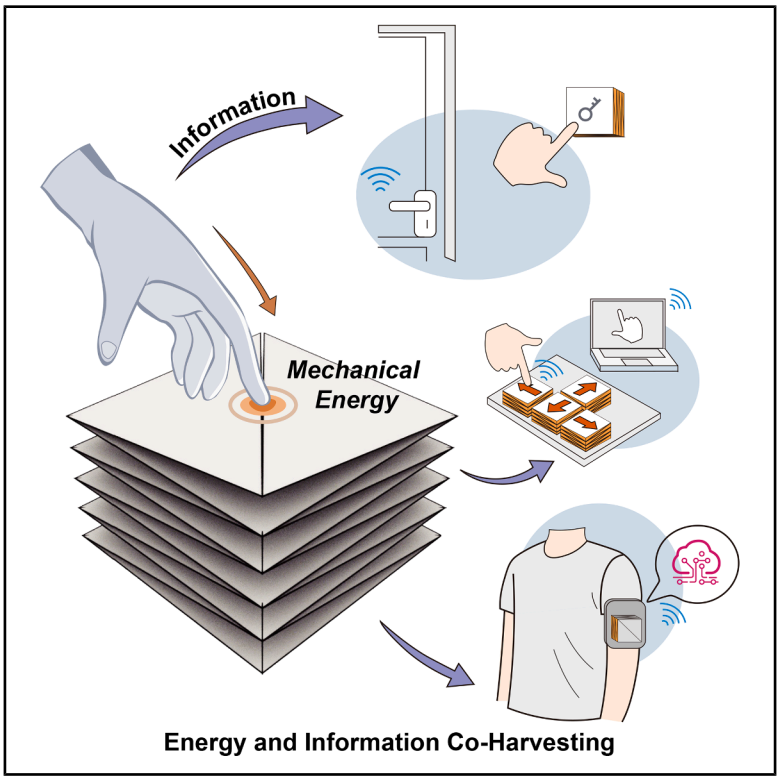

Highlights

- Foldability and effective contact area are rigorously demonstrated and derived
- Seamless integration of TENG units delivers excellent output performance
- Dedicated energy regulation enables efficient energy extraction and storage
- A synergistic energy-information harvesting system is developed

Authors

Yawei Wang, Yaozi Zheng, Yizhou Li, ..., Minyi Xu, Quanke Su, Guobiao Hu

Correspondence

guobiaohu@hkust-gz.edu.cn

In brief

Driven by the rapid growth of IoT and wearable technologies, the demand for battery-free, self-powered nodes capable of autonomous sensing and wireless data transmission has become increasingly urgent. This work introduces an origami-inspired triboelectric nanogenerator that is capable of energy and information co-harvesting from a single hand tap. By co-designing adaptive mechanical structures with efficient electrical interfacing, the proposed system enables responsive, battery-free sensing and interaction, pointing toward a new paradigm for self-powered wearable and IoT technologies.

Wang et al., 2026, Joule *10*, 102338
May 20, 2026 © 2026 The Author(s). Published by Elsevier Inc.
https://doi.org/10.1016/j.joule.2026.102338

CellPress

Please cite this article in press as: Wang et al., Origami-structured triboelectric nanogenerator for energy and information co-harvesting from a single hand tap, Joule (2026), https://doi.org/10.1016/j.joule.2026.102338

Joule

CellPress
OPEN ACCESS

Article

Origami-structured triboelectric nanogenerator for energy and information co-harvesting from a single hand tap

Yawei Wang,[1] Yaozi Zheng,[1] Yizhou Li,[1] Yi Wu,[1,2] Hao Tang,[1] Minyi Xu,[3] Quanke Su,[4] and Guobiao Hu[1,5,*]
[1]Thrust of Internet of Things, The Hong Kong University of Science and Technology (Guangzhou), Nansha, Guangzhou 511400, China
[2]Department of Mechanical Engineering, The University of Auckland, Auckland 1010, New Zealand
[3]State Key Lab of Maritime Technology and Safety, Marine Engineering College, Dalian Maritime University, Dalian 116026, China
[4]Thrust of Intelligent Transportation, The Hong Kong University of Science and Technology (Guangzhou), Nansha, Guangzhou 511400, China
[5]Lead contact
*Correspondence: guobiaohu@hkust-gz.edu.cn
https://doi.org/10.1016/j.joule.2026.102338

CONTEXT & SCALE The rapid expansion of the Internet of Things (IoT), along with the growing deployment of distributed sensing networks for applications such as structural health monitoring, environmental surveillance, and digital twins, has created an urgent demand for reliable and efficient distributed energy solutions to support long-term, maintenance-free operation of those devices. Triboelectric nanogenerators (TENGs) have emerged as a promising energy-harvesting technology due to their high integrability, structural simplicity, and strong environmental adaptability. However, despite substantial research progress in the past decade, the realization of practical battery-free TENG-powered systems remains fundamentally constrained by unresolved challenges in structural optimization, limited and intermittent energy output, inefficient energy regulation, and the lack of scalable, tightly integrated circuit architectures.

In this work, we report a diamond-tessellated, origami-inspired triboelectric nanogenerator (DT-TENG) designed for synergistic energy and information harvesting. The system is comprehensively investigated through structural design, theoretical derivation, circuit development, and experimental evaluation. By tightly integrating energy harvesting with information encoding and transmission, the proposed architecture overcomes the intermittency of ambient inputs and enables responsive, self-powered wireless sensing. The integrated system supports real-time interactive control in smart-home, gaming, and wearable sensing scenarios, establishing a modular and scalable foundation for next-generation battery-free IoT and human-machine interaction systems.

SUMMARY

Triboelectric nanogenerators (TENGs) have emerged as a promising solution for realizing self-powered Internet of Things (IoT) nodes. However, their practical deployment remains constrained by limited power output, high internal impedance, and immature system-level integration. In this paper, we present a diamond-tessellated, origami-inspired triboelectric nanogenerator (DT-TENG) that underpins a synergistic energy and information harvesting (SEIH) system. Enabled by a flat-foldable architecture, an optimized contact interface, and a plasma-treated dielectric layer, the DT-TENG achieves a peak power density of 548.33 W/m^3. A dedicated energy-regulation and impedance-matching circuit facilitates efficient energy extraction, yielding an approximately 460-fold increase in stored energy and providing a reliable power supply for system operation. Triggered by a gentle hand tap, the SEIH system supports self-powered sensing, with rapid response and high adaptability. Through energy-information co-harvesting, this work demonstrates a system-level approach to responsive, battery-free control across smart-home, human-machine interface, and wearable sensing applications.

This is an open access article under the CC BY-NC-ND license (http://creativecommons.org/licenses/by-nc-nd/4.0/).

Please cite this article in press as: Wang et al., Origami-structured triboelectric nanogenerator for energy and information co-harvesting from a single hand tap, Joule (2026), https://doi.org/10.1016/j.joule.2026.102338

INTRODUCTION

Traditional electronic sensors typically rely on chemical batteries and/or external power sources, which constrain their operational lifespans and increase maintenance complexity.[1–3] With the rapid expansion of the Internet of Things (IoT), smart wearables, and human-machine interfaces (HMIs), there is a growing demand for self-sustained sensing systems capable of providing extended, maintenance-free operation after deployment.[4] To meet this demand, energy harvesting offers a viable solution for powering sensors autonomously without reliance on traditional energy supplies. Among various energy-harvesting approaches developed, those based on piezoelectric,[2,5] thermoelectric,[6] and electromagnetic[7,8] transductions have achieved notable advancements over the past two decades. However, their relatively low power density, bulky size, and rigid operating conditions still pose challenges for seamless integration into distributed IoT nodes.

As a promising energy-harvesting solution, triboelectric nanogenerators (TENGs) offer an outstanding combination of advantages such as light weight,[9] broad material accessibility,[10] low cost,[4,11] excellent environmental adaptability,[12] and high structural flexibility.[13–16] These outstanding attributes make TENGs well-suited for integration with wearable electronics to achieve energy autonomy. TENGs operate through the coupling of contact electrification and electrostatic induction, transforming mechanical stimuli into electrical energy. Substantial efforts have been devoted to enhancing their performance—in terms of both output power and sensing resolution—via advances in structural innovation,[17–21] functional material engineering,[22–24] surface treatment,[25–27] hybrid strategies,[28–31] and interface circuitry.[32–37] By first storing the harvested energy over a certain period, TENG-based sensing systems have been widely applied in a wide range of scenarios, e.g., environmental sensing,[7,38,39] water quality assessment,[17,18] and health monitoring.[40–42] Notably, the electrical output of TENGs inherently carries both energy and motion-related signals.[43] However, existing studies primarily regard TENGs as sustainable power sources, and their information-carrying capacity remains largely underexplored.

Pioneering studies have explored the feasibility of using TENGs to realize wireless, self-powered, event-driven applications. In 2018, Mallineni et al.[44] first demonstrated a wireless TENG system utilizing electric field coupling to control smart-home devices such as chromic windows. Electric field coupling has also been used to transmit signals across different media, such as from air into water or through biological tissue. In 2020, Wang et al.[45] developed a TENG platform based on magnetic resonance coupling to realize wireless energy transfer. Following this concept, the approach was later adapted to transmit force-triggered signals, further broadening the potential of TENGs in control applications.[46] Another wireless sensing strategy was developed based on displacement currents induced by breakdown discharge.[43] It could achieve a maximum transmission distance of up to 30 m and demonstrated promising potential in HMI applications. However, these systems are still in their infancy and rely on auxiliary, bulky components like electrode plates or coils that limit their practicality. More crucially, the limited energy output of these TENGs confines them to rudimentary communication protocols, which lack the reliability and bandwidth required to interface with commercial sensor modules. This significantly limits their potential for practical and widespread use.

In this work, we propose an origami-inspired triboelectric nanogenerator featuring a diamond-tessellation structure (DT-TENG). Paired with a specialized auxiliary circuit, the system enables efficient co-harvesting of energy and information while maintaining high structural flexibility. The DT-TENG leverages the diamond-tessellation structure to effectively enhance triboelectrification and electrostatic induction within a limited, compact three-dimensional space through spatial folding operations (Figure 1A). First, a spatial triangle model was employed to systematically analyze the foldability of the diamond-tessellation origami pattern with varying angles, offering design guidelines for configuration optimization. Furthermore, flexible circuit printing was utilized to achieve seamless integration of the TENG electrodes with the substrate, while plasma treatment of the dielectric interface further enhanced output performance. The use of flexible materials and well-established fabrication techniques enables large-scale manufacturing and expands the potential for applications in various domains. In addition, the energy flow throughout the entire process was analyzed, and a dedicated energy-regulation circuit (ERC) was designed to enhance the overall output performance. Building upon this, we developed a synergistic energy and information harvesting (SEIH) system that integrates the proposed DT-TENG, the custom-tailored ERC, a storage capacitor, a sensor, and a Bluetooth low energy (BLE) system-on-chip (SoC) into a unified, compact architecture. Harnessing the inherent linkage between energy and information, the system supports a range of self-powered, event-driven applications, such as remote control, environmental sensing, and human-machine interaction. With its exceptional flexibility, strong modularity, and advanced system-level integration, the developed SEIH system offers a promising route toward energy-autonomous wearables and next-generation intelligent devices.

RESULTS

Architecture blueprint of the SEIH system

The concept of SEIH is depicted in Figure 1B. Through the coupling of triboelectrification and electrostatic induction within the designed DT-TENG, human kinetic motion is converted into electrical signals (Figure 1Bi) that carry energy and motion-related information. A custom low-power circuit efficiently regulates the energy to power the BLE SoC, while the embedded information is concurrently delivered through the BLE broadcast signals (Figure 1Bii). This SEIH system holds great potential for status monitoring and environmental sensing, with wide applications in smart homes, HMIs, and wearable devices (Figure 1Biii). Fundamentally, all these functionalities are made possible by the exclusively designed DT-TENG, which serves as the central component. Without this origami-inspired nanogenerator, neither energy nor information could be extracted from the motion. Its structural and functional

Please cite this article in press as: Wang et al., Origami-structured triboelectric nanogenerator for energy and information co-harvesting from a single hand tap, Joule (2026), https://doi.org/10.1016/j.joule.2026.102338

CellPress
OPEN ACCESS

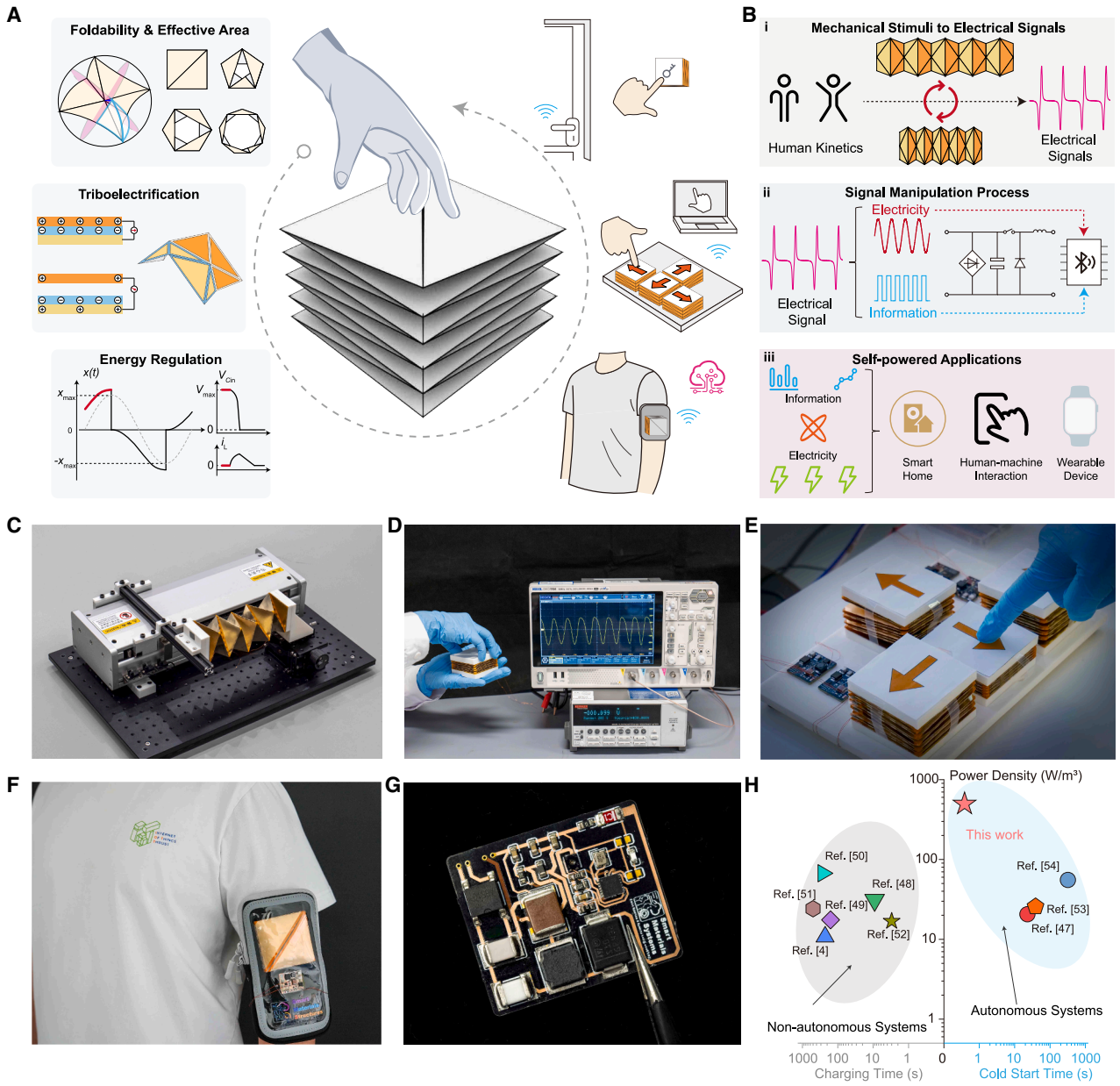

Figure 1. Design concept and architecture of an origami-based TENG for self-powered wireless sensing

(A) Conceptual illustration of a foldable, origami-inspired triboelectric nanogenerator (DT-TENG), enabling an enlarged contact area and compactness for integration into smart wearable electronics or IoT platforms.

(B) The information-energy co-transmission architecture: (i) human kinetic motion is converted into electrical signals via triboelectrification; (ii) auxiliary circuitry converts the raw signal into usable information; and (iii) the harvested energy and embedded logic support self-powered applications such as smart-home control, wearable electronics, and human-machine interaction.

(C) Photograph of the DT-TENG mounted on a programmable linear motor platform for mechanical excitation and performance testing.

(D) Measurement setup and demonstration of the electrical signal produced by the DT-TENG.

(E) Demonstration of four DT-TENGs integrated with circuitry for use in human-machine interaction applications.

(F) A wearable prototype of the SEIH system embedded in a soft arm bag, suitable for on-body sensing.

(G) Close-up image of the flexible printed circuit board (FPCB) for the SEIH system, responsible for rectification, energy regulation, and wireless sensing task execution.

(H) Comparison of peak power density and cold-start response time between the SEIH system and state-of-the-art designs from the literature.[4,47–54] The highlighted blue region denotes the performance range of autonomous systems, while the gray-outlined region corresponds to non-autonomous sensing platforms.

See more details in Table S1.

design directly enables the seamless integration of motion transduction with electrical output. During operation, the DT-TENG, folded into a multilayer stacked structure, can convert reciprocating motion, such as human kinematics, into electrical signals for both energy-harvesting and sensing applications (Figures 1C and 1D).

To fully exploit the energy-harvesting potential of the DT-TENG, we developed a dedicated interface circuit that regulates energy flow, conducts sensing, and supports wireless data transmission, thereby achieving self-powered applications (Figures 1E–1G). Owing to the ultra-low-power feature of the custom-designed circuit, the DT-TENG-powered SEIH system realizes energy-autonomous sensing, such as motion perception and environmental monitoring, with a negligible cold-start time and uninterrupted BLE data broadcasting. In comparison with the self-powered sensing systems reported in the literature,[4,47–54] our design exhibits significantly improved responsiveness and superior instantaneous power density (Figure 1H; Table S1). This enhanced performance is attributed to the well-integrated architecture of the SEIH system and the coordinated optimization across the energy harvester, the ERC, and the SoC. These features make DT-TENG a promising candidate for event-driven, low-duty-cycle sensing scenarios in wearable electronics and IoT environments.

Origami morphology and planar foldability

The crease pattern folding governs the output performance of the origami-inspired TENG by facilitating a transformation from a simple, flat 2D sheet to a 3D structure, which then collapses back into a multilayered 2D configuration with interleaved planar surfaces. To analyze this transformation and assess the feasibility of re-collapsing into a layered 2D configuration, we first examine the developability and flat-foldability of the diamond-patterned origami, which features six creases indicated by red (mountain) and blue (valley) dashed lines (Figure 2A). Six creases converge at a common vertex, dividing the sheet into six sectors, each defined by an angle $\alpha_{i,(i+1)}$. The dihedral angles between adjacent panels connected by the crease are defined as φ_i, where i is the index of the crease, ranging from 1 to 6 (when $i = 6$, $i + 1$ cycles back to 1). As a fundamental geometric constraint, developability ensures that the origami structure can be unfolded into a flat plane. This condition can be mathematically expressed as:

$$\alpha_{1,2} + \alpha_{2,3} + \cdots + \alpha_{n,1} = 2\pi. \quad \text{(Equation 1)}$$

Foldability refers to an origami structure's capacity to collapse into a planar form with self-overlapping facets. The geometric constraints at a single vertex are governed by the Kawasaki-Justin theorem (Equation 2) and the Maekawa-Justin theorem (Equation 3), which can be expressed as:

$$\sum_{i\_odd} \alpha_{i,i+1} = \sum_{i\_even} \alpha_{i,i+1}, \quad \text{(Equation 2)}$$

$$M - V = \pm 2, \quad \text{(Equation 3)}$$

where *i_odd* and *i_even* denote the indices of alternating angle pairs around the vertex, M is the number of mountain folds, and V is the number of valley folds.

Loop-closure constraints of equivalent spatial linkages have been used in previous studies to assess and prove the rigid foldability of origami structures.[55,56] In this work, we apply these constraints to our diamond-patterned origami design, with the resulting formulation expressed as follows:

$$Q_{1,2}Q_{2,3}Q_{3,4}Q_{4,5}Q_{5,6}Q_{6,1} = I_3, \quad \text{(Equation 4)}$$

where the matrix $Q_{i,(i+1)}$ takes the following form:

$$Q_{i,(i+1)} = \begin{bmatrix} \cos\theta_i & \sin\theta_i & 0 \\ -\cos\alpha_{i,(i+1)}\sin\theta_i & \cos\alpha_{i,(i+1)}\cos\theta_i & \sin\alpha_{i,(i+1)} \\ \sin\alpha_{i,(i+1)}\sin\theta_i & -\sin\alpha_{i,(i+1)}\cos\theta_i & \cos\alpha_{i,(i+1)} \end{bmatrix}. \quad \text{(Equation 5)}$$

This transformation matrix is used to convert expressions from the ith coordinate system to the $(i + 1)$-th coordinate system, where θ_i represents the rotation angle between two facets connected by a crease, defined as a revolute joint Z_i (Figure 2B). Considering the symmetry of the tessellated pattern, the following conditions can be derived:

$$\begin{cases} \alpha_{3,4} = \alpha_{4,5} = \alpha_{6,1} = \alpha_{1,2} \\ \alpha_{2,3} = \alpha_{5,6} = \pi - 2\alpha_{1,2} \\ \theta_1 = \theta_4 \\ \theta_2 = \theta_3 = \theta_5 = \theta_6 \end{cases}. \quad \text{(Equation 6)}$$

By evaluating and solving Equation 4, the relationship between the two angles φ_1 and φ_2 during the folding process for various values of angle $\alpha_{1,2}$ is derived as Equation 7 (Figure 2C and Note S1).

$$\varphi_1 = \arccos\left(\frac{(2\cos(\varphi_2) - 2)\cos\left(\alpha_{1,2}\right)^2 + (2\cos(\varphi_2) - 2)\cos\left(\alpha_{1,2}\right) + \cos(\varphi_2)}{(2 - 2\cos(\varphi_2))\cos\left(\alpha_{1,2}\right)^2 + (2 - 2\cos(\varphi_2))\cos\left(\alpha_{1,2}\right) + 1}\right). \quad \text{(Equation 7)}$$

Please cite this article in press as: Wang et al., Origami-structured triboelectric nanogenerator for energy and information co-harvesting from a single hand tap, Joule (2026), https://doi.org/10.1016/j.joule.2026.102338

CellPress
OPEN ACCESS

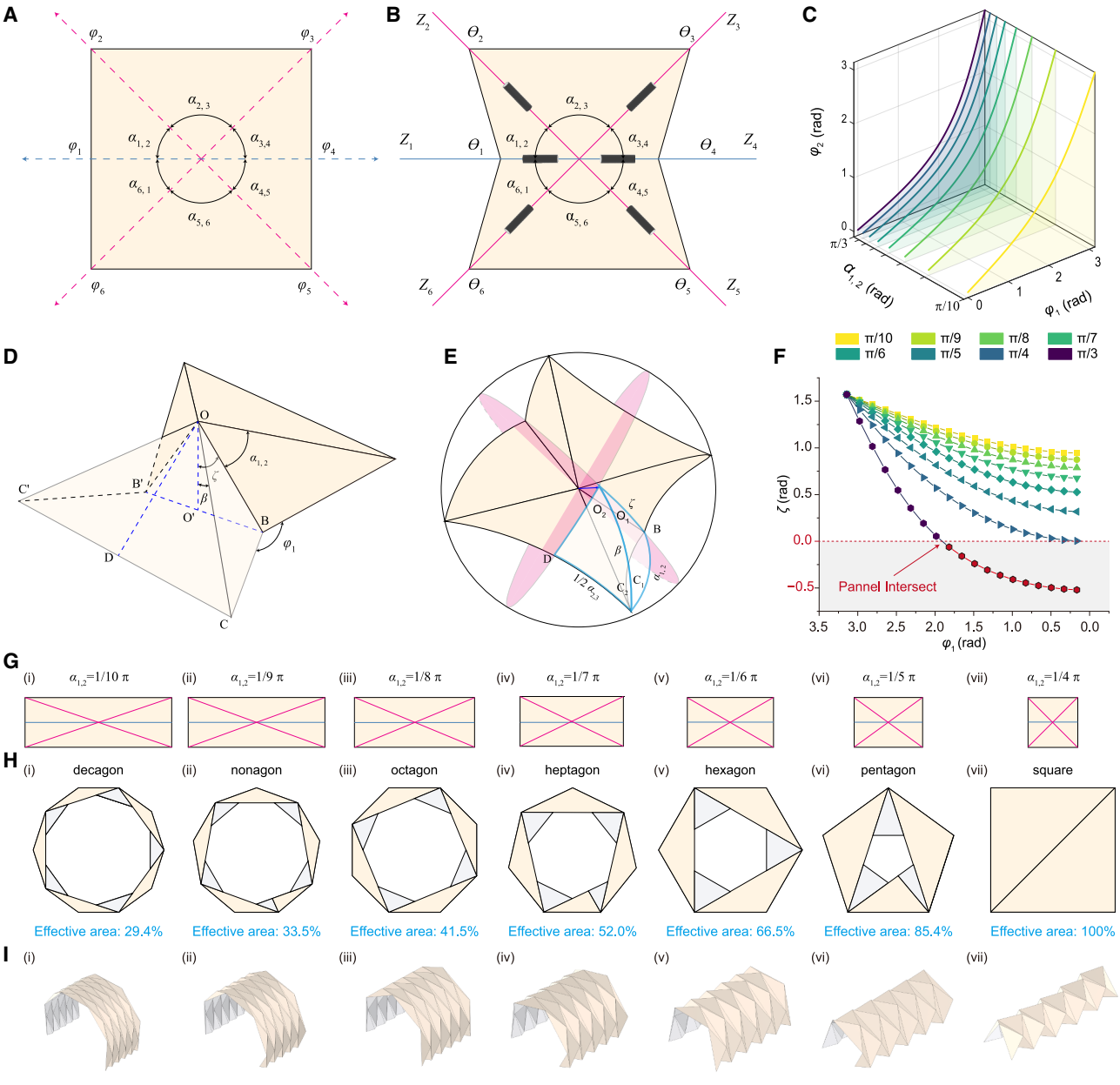

Figure 2. Rigid foldability and effective area enlargement effect of the origami-inspired TENG

(A) Schematic of the diamond origami pattern featuring a single vertex and six creases. Mountain and valley creases are denoted by blue and red dashed lines, respectively.

(B) Definition of geometric parameters and mechanical joints for the diamond origami following Denavit-Hartenberg (D-H) notation.

(C) Relationships between the dihedral angles of the diamond origami with different sector angles $\alpha_{1,2}$.

(D) Perspective view of a partially folded diamond origami.

(E) Spherical triangles used to compute the relationship between θ_i and ζ.

(F) Numerical results showing the variation of the folding angle ζ as a function of θ_i for different values of sector angle $\alpha_{1,2}$.

(G) Unfolded, flat patterns of the diamond origami with different values of sector angle $\alpha_{1,2}$, ranging from $\pi/10$ to $\pi/4$.

(H) Top views of fully folded tessellated structures with polygonal geometries ranging from a decagon to a square. The blue annotations indicate the effective areas of the configurations (see methods section for details).

(I) Axonometric view of the corresponding partially folded origami structures with $n = 5$.

Please cite this article in press as: Wang et al., Origami-structured triboelectric nanogenerator for energy and information co-harvesting from a single hand tap, Joule (2026), https://doi.org/10.1016/j.joule.2026.102338

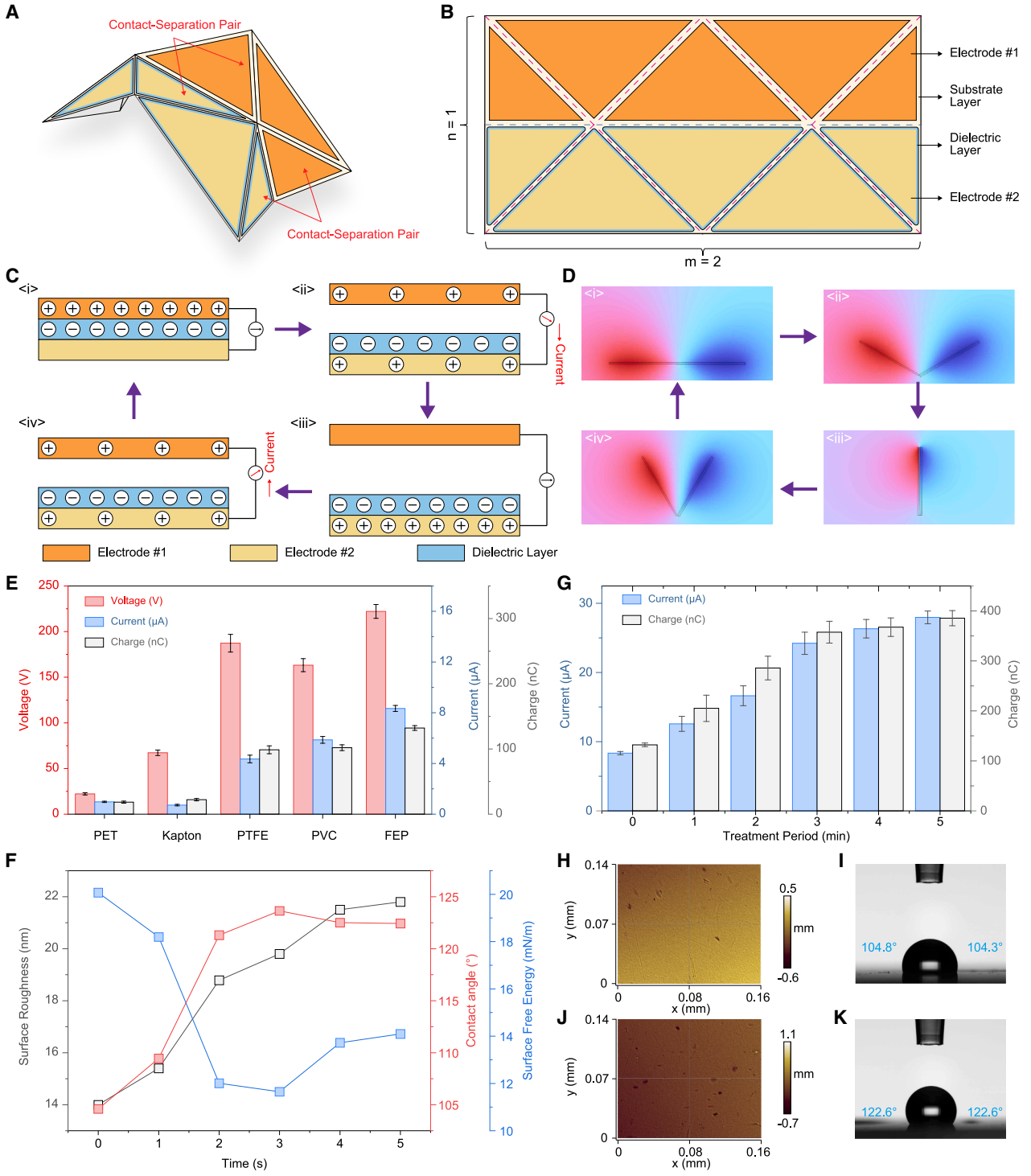

Figure 3. Working mechanism, materials selection, and surface treatment effects of the DT-TENG

(A) Illustration of the partially folded DT-TENG, highlighting the contact-separation electrode pairs.

(B) Pattern diagram of the DT-TENG with $n = 1$ and $m = 2$. Dimensional specifications and photographs are available in Figures S1 and S2.

(C) Fundamental working principle of the contact-separation mode TENG, illustrating the sequential charge transfer and current generation during mechanical deformation.

(D) Finite element (FE) simulation of the dynamic potential distribution between the two electrodes over one contact-separation cycle.

(legend continued on next page)

However, these methods provide only necessary yet not sufficient conditions to ensure foldability.[57] In this work, based on the spatial triangle model,[58] we introduce a novel approach to further investigate the folding behavior of the origami structure.

Figure 2D presents a schematic of the diamond origami structure. Connect points B and B', and draw a perpendicular line from point O to line BB'. Let ζ denote the angle between lines OO' and OB, and let β represent the angle between OO' and OC. Let D be the midpoint of line CC', and denote the angle $\angle$DOC as $\alpha_{1,2}/2$. The values of ξ and β are positive, with a value of 90° representing the fully unfolded state of the origami pattern. Spherical triangles are used to establish the relationships between ζ and φ_1 for different sector angles (Figure 2E). To facilitate computation, the sphere on which all these triangles lie is assumed to have a unit radius. According to the cosine and sine laws of spherical trigonometry, along with the condition that follows $D = \pi/2$, $O_1 + O_2 = \pi/2$, and $B = \pi - \theta_i/2$, the following relations can be derived (Note S2):

$$\begin{cases} \tan O_1 = \tan \alpha_{1,2} \cdot \sin\left(\dfrac{\theta_1}{2}\right) \\ \sin \beta = \dfrac{\sin \alpha_{1,2} \cdot \sin \dfrac{\theta_1}{2}}{\sin O_1} \\ \cos \beta = \cos \alpha_{1,2} \cdot \cos \zeta + \sin \alpha_{1,2} \cdot \sin \zeta \cdot \cos \dfrac{\theta_1}{2} \end{cases}. \quad \text{(Equation 8)}$$

Figure 2F illustrates the variation of ζ with respect to φ_1 as the sector angle varies from $\pi/10$ to $\pi/3$. When $\varphi_1 = \pi$, ζ reaches $\pi/2$, indicating that the origami structure is fully folded. As φ_1 varies toward 0, ζ correspondingly decreases. When $\alpha_{1,2} = \pi/4$, both φ_1 and ζ become zero, marking the critical sector angle of the origami structure. If $\alpha_{1,2}$ exceeds $\pi/4$, ζ becomes negative during the folding process, indicating that lines OB and OB' (Figure 2D) intersect, thereby preventing the structure from folding into a flat, planar configuration. Therefore, the crease pattern exhibits rigid foldability only when $\alpha_{1,2}$ lies within the interval $(0, \pi/4)$. Furthermore, by tessellating the diamond pattern, a three-dimensional scale-closed structure can be constructed. The relationship between the number of sides and angles of the polygon is given as follows[59]:

$$\begin{cases} \gamma = \dfrac{2\pi}{\pi - \alpha_{2,3}} = \dfrac{\pi}{\alpha_{1,2}} \\ m = \dfrac{1}{2}\gamma \end{cases}, \quad \text{(Equation 9)}$$

where γ is the number of polygon sides formed after the origami pattern is folded, which can be calculated for the corresponding $\alpha_{1,2}$. The parameter m represents the number of origami tessellations in a single row. We constructed various origami patterns with $\alpha_{1,2}$ ranging from $\pi/10$ to $\pi/4$ and examined their corresponding flat-folded states (Figures 2G and 2H). Figure 2I and Video S1 demonstrate the folding and developing process of the origami patterns. The results clearly show that foldability fails when $\alpha_{1,2} = \pi/3$, while configurations with other sector angles can be folded and developed completely.

Working mechanism and performance assessment

Based on triboelectrification and electrostatic induction coupling, TENGs convert external mechanical stimuli into electrical energy. Their power outputs are governed by the surface charge density, which is determined by the type of materials used and the contact area. Therefore, for given electrode and dielectric materials, the performance of a TENG can be improved by enlarging the interface area where the triboelectric charge transfer takes place. Considering that other origami patterns form a geometric hollow at the center when fully folded, resulting in a reduction in effective area (Figures 2H and 2I), the pattern with $\alpha_{1,2} = \pi/4$ was selected for its maximum area utilization. In fabricating the DT-TENG, metal is deposited onto the substrate layer in two separate regions, forming two electrodes, #1 and #2, respectively (Figures 3A and 3B). Electrode #1 serves as both an electrode and a tribopositive material. Meanwhile, a dielectric film is coated onto the surface of electrode #2, functioning as a tribonegative material to capture electrons from electrode #1. By using flexible circuit printing, we developed an integrated fabrication process for the DT-TENG substrate and electrodes, ensuring high flexibility and smooth flat-foldability (see methods section for details).

During the folding process of the origami pattern, relative motion and interfacial contact take place between electrode #1 and the dielectric layer over their planar regions, facilitating both internal charge induction and external charge transfer in the DT-TENG (Figure 3A). Figures 3C and 3D present the fundamental working mechanism of the TENG through illustrative schematics and finite element (FE) simulations. Triboelectrification, the primary driving mechanism of TENGs, occurs when two different materials come into contact (Figure 3Ci). Electrostatic induction follows as charges redistribute in response to electrostatic forces within an electric field (Figures 3Cii–3Civ). The coupling of triboelectrification and electrostatic induction results in a charge transfer through an external circuit, generating a conduction current. FE results indicate that the potential gradient between the contact-separation pair develops asymptotically during the contact or separation process (Figure 3D), thereby promoting directional charge transfer across the electrodes.

(E) Comparison of output voltage and current performance of the DT-TENG fabricated with different dielectric materials, including polyethylene terephthalate (PET), Kapton, polytetrafluoroethylene (PTFE), polyvinyl chloride (PVC), and FEP. Bar heights represent mean values; error bars indicate standard deviations (SD) from five independent tests ($n = 5$).

(F) Surface roughness, contact angle, and surface free energy of the dielectric layer before and after 1–5 min of plasma treatment. Bar heights represent mean values; error bars indicate SDs from five independent tests ($n = 5$).

(G) Short-circuit current (I_{sc}) and charge output (Q_{sc}) of the DT-TENG with the dielectric layers before and after 1–5 min of plasma treatment, showing a marked enhancement in performance after treatment.

(H and I) Surface morphology and water contact angle of the FEP film before plasma treatment.

(J and K) Surface morphology and water contact angle of the FEP film following a 3-min plasma treatment.

Please cite this article in press as: Wang et al., Origami-structured triboelectric nanogenerator for energy and information co-harvesting from a single hand tap, Joule (2026), https://doi.org/10.1016/j.joule.2026.102338

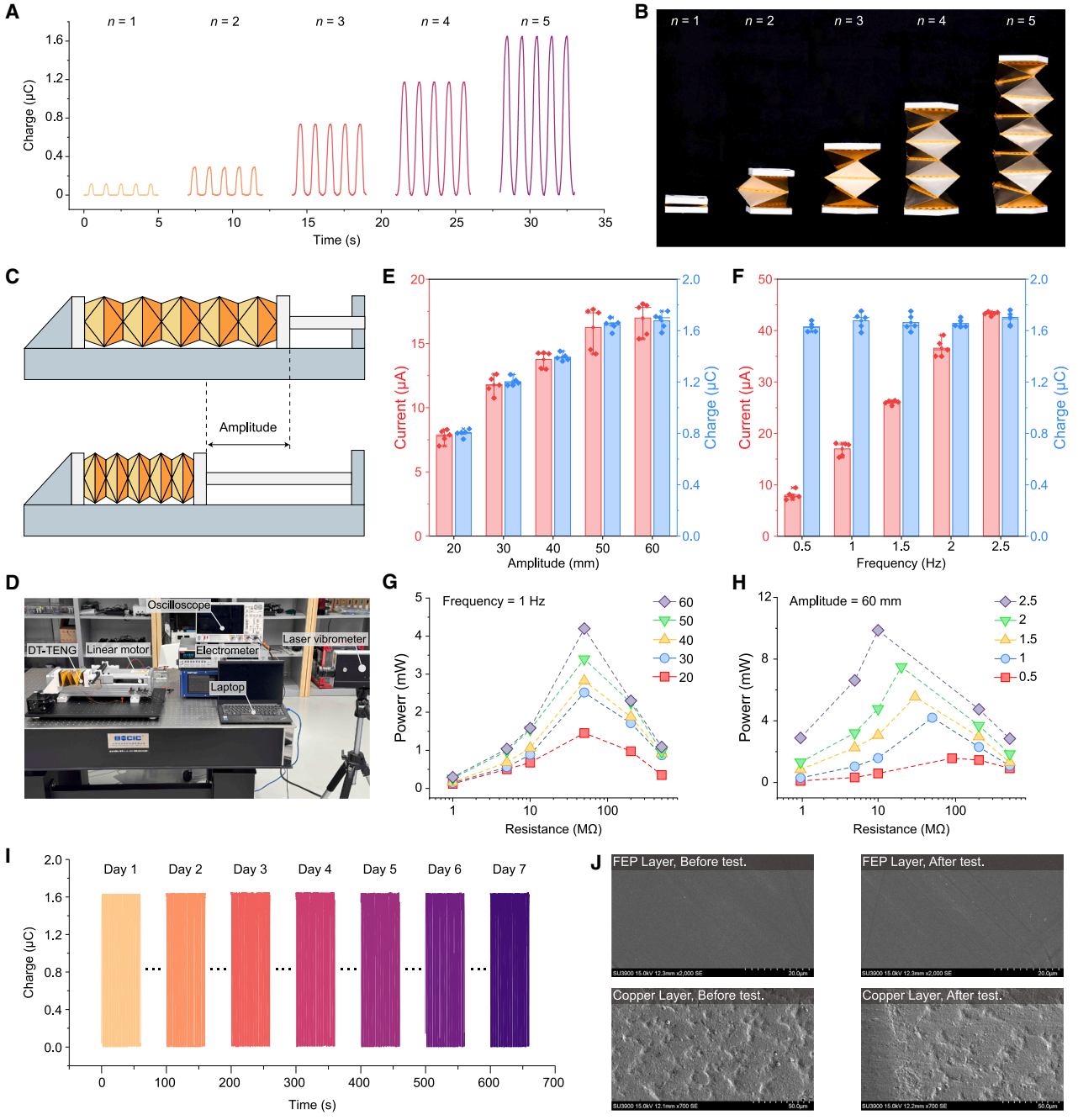

Figure 4. Electrical output performance, parameter dependence, and durability of the DT-TENG

(A) Short-circuit charge output (Q_{sc}) of the DT-TENG with varying numbers of stacked layers (n = 1–5), showing enhanced performance with increasing layer count.

(B) Photographic comparison of the DT-TENG prototypes with n varying from 1 to 5.

(C) Schematic diagram of the experimental setup.

(D) Photograph of the experimental setup, including the linear motor, data acquisition system, and the laser vibrometer.

(E and F) Electrical output (current and charge) of the DT-TENG with n = 5 under different excitation amplitudes (E) and frequencies (F). Bar heights represent mean values; error bars indicate SDs from five independent tests (n = 5).

(G and H) Peak power output of the DT-TENG as a function of external load resistance, under different excitation amplitudes (G) and frequencies (H), identifying optimal impedance for maximum power transfer.

(legend continued on next page)

Various dielectric materials with negative triboelectric properties were coated onto electrode #2 (Figure 3B), and their output characteristics, including open-circuit voltage (V_{oc}), short-circuit current (I_{sc}), and short-circuit charge (Q_{sc}), were evaluated (Figure 3E). Among them, the DT-TENG using fluorinated ethylene propylene (FEP) as the dielectric material exhibits the best output performance, achieving 210 V in V_{oc}, 1.2 μA in I_{sc}, and 110 nC in Q_{sc}, thereby justifying its selection for subsequent experimental studies. In addition to the triboelectric charge affinity, surface micro-structuring offers an effective means to boost TENG output by enlarging the contact area. In this work, plasma treatment was applied to the FEP film to enhance the triboelectrification effect (Figure S3). Figure 3F presents the arithmetical mean height (surface roughness, Sa), water contact angle, and surface free energy of the FEP films before and after plasma treatment. The results show that the Sa value of the FEP film gradually increased with plasma exposure time (from 1 to 5 min). However, when the treatment duration exceeded 3 min, the water contact angle and surface free energy showed a reversal trend. This is likely because plasma treatment initially increases surface roughness, but prolonged exposure causes chemical changes that render the films more hydrophilic. The triboelectric output characteristics exhibited a similar trend (Figure 3G), indicating that a 3-min plasma treatment achieved a balance between physical and chemical effects; thus, this duration was adopted. Figures 3H–3K display the surface morphology images and water contact angles of the FEP film before and after 3-min plasma treatment, respectively, clearly illustrating the evolution of surface roughness and wettability (additional results for other treatment durations are provided in Figures S4 and S5).

The DT-TENG design enables further expansion and enhancement by increasing the number of layers n (Figure 2I). Figure 4A presents the Q_{sc} characteristics of the DT-TENG prototypes with n = 1 to 5 (corresponding prototypes in Figures 4B and S6), demonstrating that voltage output increases with the number of layers. Considering the power requirements of electronic devices, the D-TENG with n = 5 was selected for comprehensive performance evaluation. To characterize the electrical output of the DT-TENG, tests were conducted under various excitation conditions using the setup shown in Figures 4C and 4D. The results show that, at 1 Hz, both current and charge outputs increase with higher excitation amplitudes (Figures 4E, S7, and S8). This is because higher excitation amplitudes promote more effective folding/unfolding of the origami structure, thereby enhancing surface interaction between contact-separation pairs and facilitating greater charge transfer. Frequency also has a significant impact on the output response of the DT-TENG (Figures 4F, S9, and S10). With the amplitude fixed at 60 mm, the transferred charge remains nearly constant, while the current increases with frequency rises. This occurs because TENG's charge output is almost frequency-independent,[60,61] whereas current, as the first time derivative of charge, is inherently influenced by the excitation frequency.

We further characterized the optimal impedance and maximum power density of the DT-TENG under various frequencies and amplitudes (Figures 4G, 4H, S11, and S12). Notably, unlike the effect of excitation amplitude, increasing the frequency not only enhances the peak power output but also reduces the optimal resistance, which is a trend consistent with previous studies.[62] At an excitation amplitude of 60 mm and a frequency of 2.5 Hz, the DT-TENG achieves an instantaneous power output of 9.87 mW, corresponding to a power density of 548.33 W/m^3 (refer to the methods section for details). To evaluate the long-term durability and environmental adaptability of the DT-TENG, the device was placed in an environmental simulation chamber to assess its output characteristics under the controlled conditions of 18°C–30°C and 30%–70% relative humidity. The results indicate that temperature variations within this range have a negligible impact on the DT-TENG's electrical output (Figure S13). However, as the humidity increased, the charge transfer capacity of the DT-TENG decreased slightly (Figure S14). Furthermore, with the temperature controlled between 20°C–25°C and the relative humidity between 40%–60%, periodic excitations were applied using a test bench, and the output charge was recorded daily. Over a 1-week testing period, the DT-TENG maintained consistent performance with no observable degradation, confirming its excellent durability and environmental resilience (Figure 4I). Moreover, scanning electron microscopy (SEM) images in Figure 4J compare FEP and electrode #1 surfaces before and after testing. The minimal material wear observed further confirms the DT-TENG's strong durability. A comparison of these key parameters with those of previously reported origami-based TENGs is provided in Table S2.

Energy regulation via impedance engineering

Although TENGs deliver high instantaneous power, they suffer from drawbacks like low current output and high internal impedance,[18] which significantly restrict their effectiveness in powering external loads. To address these challenges and exploit the full potential of our DT-TENG, we introduce a dedicated energy-regulation strategy to mitigate the high internal impedance effect. This strategy consists of three operational phases: an energy accumulation phase, an energy extraction phase, and a freewheeling phase. High internal impedance is a fundamental drawback of TENGs. It not only leads to substantial voltage drops under load but also impairs energy transfer efficiency, as a considerable portion of the harvested energy is dissipated within the device rather than being delivered to external loads. Additionally, the high impedance makes it difficult to achieve proper impedance matching with practical electronic devices, thereby limiting power delivery and reducing impedance compatibility. This dedicated

(I) Long-term output stability of the DT-TENG over 7 consecutive days of operation at an excitation of 1 Hz and 60 mm, demonstrating consistent charge output (Q_{sc}).

(J) Scanning electron microscopy (SEM) images of the FEP and copper electrode layers before and after 7 days of cyclic operation, showing minimal surface degradation and good material durability.

See also Figures S7–S12.

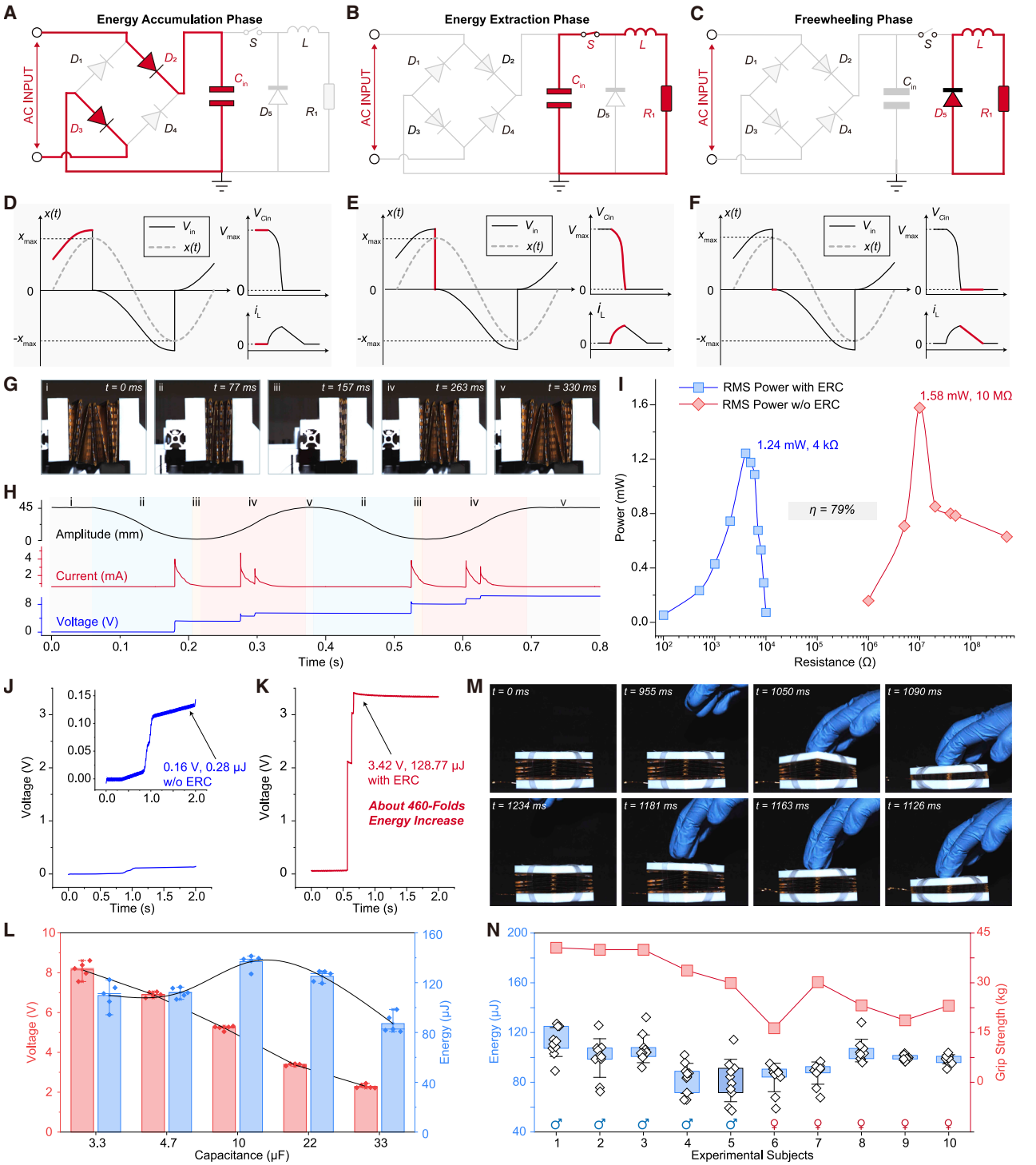

Figure 5. Energy-regulation strategy for the DT-TENG and its practical usability

(A–C) Circuit diagrams showing three phases: (A) the energy accumulation phase, (B) the energy extraction phase, and (C) the freewheeling phase.

(D–F) Corresponding electrical waveforms for the three phases over a half cycle. $x(t)$, x_{max}, and $-x_{max}$ represent the instantaneous, maximum, and minimum displacements, respectively. V_{Cin} denotes the voltage across the capacitor C_{in}, and i_L denotes the current flowing through the inductor L.

(G and H) Sequential images and corresponding output waveforms during the movement of the DT-TENG integrated with the energy-regulation circuit (ERC) under excitation by a linear motor.

(legend continued on next page)

Please cite this article in press as: Wang et al., Origami-structured triboelectric nanogenerator for energy and information co-harvesting from a single hand tap, Joule (2026), https://doi.org/10.1016/j.joule.2026.102338

energy-regulation scheme effectively lowers the DT-TENG's internal impedance, thereby enabling more efficient energy extraction and improved voltage stability. This enhancement greatly improves compatibility with low-impedance load devices and is critical for maximizing power delivery in real-world, event-driven, and self-powered sensing systems.

To implement this strategy, we designed a circuit that first rectifies the AC output of the DT-TENG and stores the harvested energy in a high-voltage capacitor. In the energy accumulation phase, both switch S and diode D_5 remain off, preventing any premature energy delivery to the electronic load (Figures 5A and 5D). The general V-Q-x relationship of TENGs indicates a strong correlation between output voltage and mechanical displacement.[60] Accordingly, the DT-TENG delivers its peak voltage when its displacement reaches maximum. At this synchronized moment, switch S is turned on, and energy stored in capacitor C_{in} is swiftly channeled into inductor L, thus initiating the energy extraction phase (Figures 5B and 5E). The ultra-short conduction time for energy extraction results in a sharp rise in current, which effectively alleviates the impedance mismatch caused by the capacitive nature of the TENG. After this, switch S is turned off, and inductor L releases its stored energy to the external load via diode D_5 (Figures 5C and 5F). During the second half of the cycle, a similar sequence of three phases occurs, with reversed voltage polarity and an altered rectification path, as illustrated in Figure S15.

Based on the outlined strategy, we fabricated an ERC to efficiently manage and channel the energy harvested by the DT-TENG (Figure S16). Note S3 offers a comprehensive description of the roles of each component in the ERC, as well as the component selection methodology. Figures 5G and 5H and Video S2 illustrate the displacement, load current, and capacitor charging behavior of the DT-TENG under linear motor excitation. Unlike conventional sources that supply steady current outputs, the DT-TENG integrated with the ERC delivers current to the back-end circuitry only when the switch S is on. At that moment, the voltage across the storage capacitor C_{in} is instantly extracted, aligning precisely with the intended design of the proposed energy-regulation strategy. The root mean square (RMS) power outputs of the DT-TENG with and without using the ERC are evaluated and compared. Although the presence of the ERC causes a slight reduction in the optimal RMS power (indicating an efficiency of 79%, Figure 5I), it significantly lowers the internal impedance from 10 MΩ to 4 kΩ, thereby improving the DT-TENG's compatibility with commercial electronic devices. This benefit is firmly substantiated by the voltage charging performance of the DT-TENG integrated with the ERC, which shows a 460-fold increase in energy collected within a single working cycle (Figures 5J and 5K). The observed substantial enhancement stems from the ERC's function to regulate current more effectively and facilitate impedance matching with the load.

We further studied the charging voltage and energy output of the DT-TENG, with the ERC using different storage capacitors. Each measurement was conducted under a single activation applied by a linear motor, and the harvested energy was quantified in microjoules (Figures 5L and S17). Using the ERC with a capacitor of 10 μF, the collected energy from just a single activation cycle reaches an average value of 136.87 μJ. The effects of excitation frequency and amplitude were also investigated (Figures S18–S20). The results indicate that variations in frequency have a minor impact on charging performance. However, when the excitation amplitude falls below 20 mm, the ERC fails to extract charges to the capacitor due to the low output voltage from the DT-TENG. To address this limitation and ensure both structural stability and user-friendly operation, the DT-TENG was packaged into a modularized unit (Figure S21). Rigid support was achieved by attaching 3D-printed blocks to the top and bottom of the flexible DT-TENG, while plastic strips on all four lateral sides maintained structural balance and alignment. The gap between the blocks was set to 25 mm to preserve the proper functioning of the ERC. Mechanical performance of the packaged DT-TENG was further examined using a universal testing machine (Figure S22; Video S3). The device delivered ~1.28 μC of transferred charge under a pressing force of <10 N with a displacement of up to 13 mm.

This modular design facilitates user-friendly, hand-driven excitation and provides compatibility with various practical applications (Figures 5M and S23; Video S4). Figure 5N illustrates the energy outputs of the DT-TENG across ten independent trials, each under a single hand-tap actuation by individual participants (see details in Figures S24–S33). The variations observed in the results may arise from factors such as grip strength differences in testers, actuation inconsistencies (e.g., angle, force, and contact area), and tolerances among tested DT-TENG prototypes. Despite the observed fluctuations, the energy harvested per cycle remains sufficient to support a broad range of IoT applications.

Battery-free, event-driven sensing and communication

To achieve wireless sensing both triggered and powered by a single mechanical actuation, we developed an SEIH system that integrates a DT-TENG, an ERC, a storage capacitor ($C_{storage}$), and a BLE SoC (Figures 6A and S34). Through the seamless integration, efficient energy capture, adaptive regulation, event-driven sensing, and wireless data transmission are achieved, even under very minimal energy input. With just

(I) RMS power output of the DT-TENG as a function of external resistance, comparing results with and without using the ERC, under an excitation amplitude of 50 mm and frequency of 2 Hz.
(J and K) Capacitor charging curves for the DT-TENG with and without the ERC, using a 22 μF capacitor, under a single-stroke excitation (amplitude, 45 mm; peak velocity, 540 mm/s; constant acceleration, 6,480 mm/s^2).
(L) Charging voltage and corresponding energy output of the DT-TENG with ERC for different capacitors during a single operation cycle. Bar height indicates mean values; error bars represent SD from n = 5 independent tests (amplitude, 30 mm; maximum velocity, 360 mm/s; constant acceleration, 4,320 mm/s^2).
(M) Sequential photos of the movement process of the DT-TENG triggered by a human hand, demonstrating user-interactive energy harvesting.
(N) Harvested energy and corresponding grip strength measurements of 10 participants (5 female and 5 male participants; Table S3), visualized using box plots with interquartile ranges and whiskers indicating ±1 SD, based on ten independent tests. The raw charging curves are available in Figures S24–S33.
See also Figures S15 and S17.

Please cite this article in press as: Wang et al., Origami-structured triboelectric nanogenerator for energy and information co-harvesting from a single hand tap, Joule (2026), https://doi.org/10.1016/j.joule.2026.102338

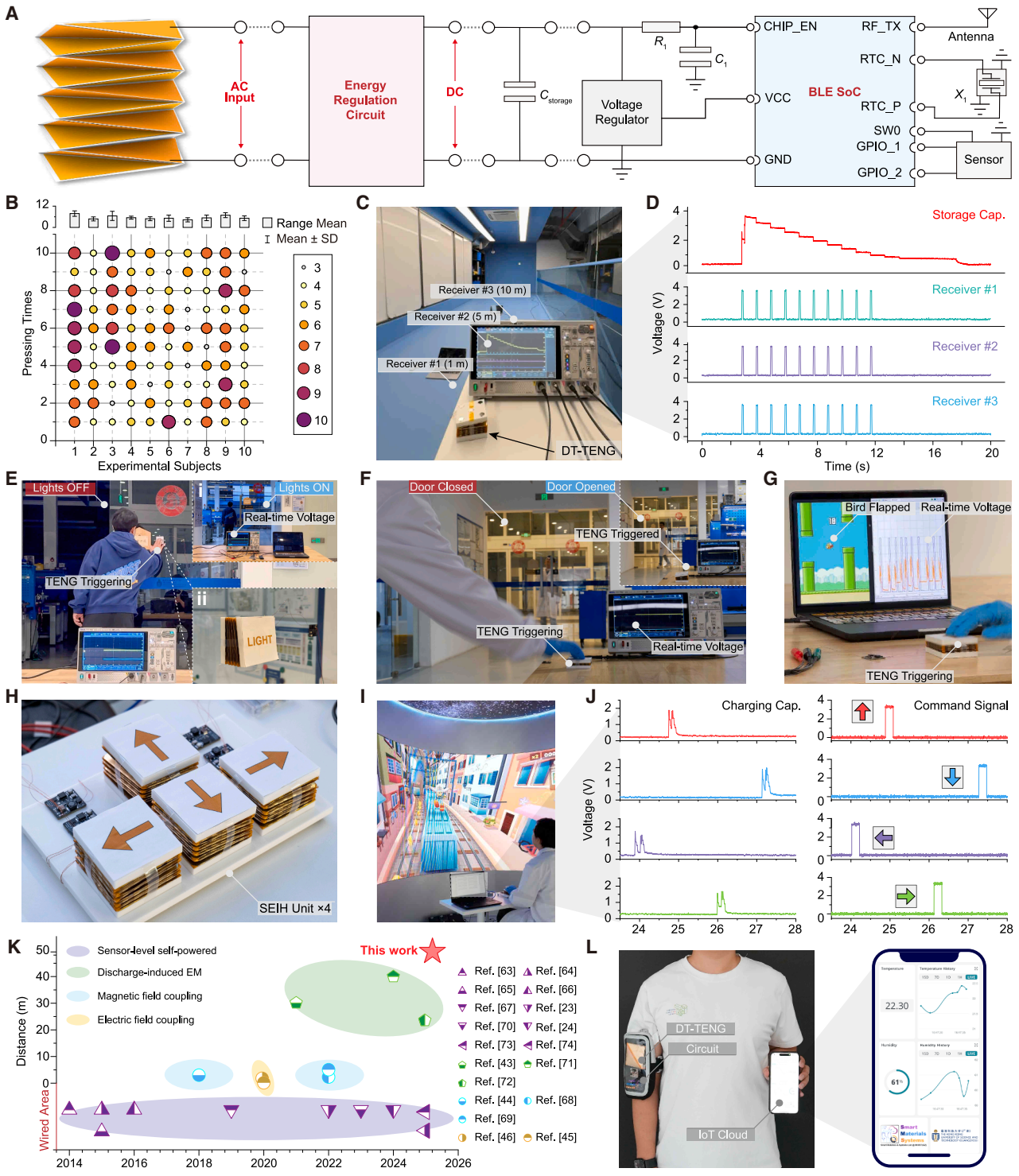

Figure 6. Demonstration of the SEIH system: Self-powered energy-information fusion system and its practical applications

(A) System architecture diagram illustrating the process of energy harvesting, energy regulation, and wireless sensing and transmission. The detailed circuit implementation is shown in Figure S34.

(B) Heatmap showing the number of successful packets transmitted by the SEIH system per hand tap across ten human participants. The circle size and color indicate the count (ranging from 3 to 10), with larger and darker circles indicating higher success rates. The inset bar plot shows the mean values and SDs of the packet counts received from all ten participants. See also Figures S36–S45.

(C) Experimental setup for testing wireless transmission distance, with three receivers positioned at 1, 5, and 10 m from the SEIH system.

(legend continued on next page)

a single gentle hand tap applied to the DT-TENG of the SEIH system, the BLE SoC was successfully powered to broadcast packets, with eleven packets detected (Figure S35). Furthermore, ten volunteer participants were recruited, each performing ten hand-tap trials (Figures 6B and S36–S45). In every trial, the Bluetooth receiver reliably received the transmitted signals from the SEIH system, with the number of BLE packets detected per hand tap ranging from three to ten. This astonishingly demonstrates that such a trivial mechanical action—a single gentle hand tap—on the DT-TENG can generate sufficient energy for wireless communication and real-time motion detection. We further assessed the SEIH system's wireless transmission distance (Figures 6C, 6D, and S46). In response to a single hand-tap excitation, the SEIH system could transmit ten BLE advertisement packets in the best-case scenario, with all packets successfully received by three distinct receivers located at distances of 1, 5, and 10 m within a laboratory environment (Figure 6D; Video S5). In indoor environments with minimal obstructions, the BLE signal from the SEIH system remained detectable at distances of up to 50 m (Figure S47). To further examine the impact of environmental variations on the SEIH system, hand-tapping tests were conducted under controlled conditions (Figures S48 and S49). The results show that the SEIH system maintains robust performance and stability across varying temperature and humidity conditions. Moreover, the robustness of the SEIH system was evaluated under a range of mechanical loading conditions (Figures S50–S52; Videos S6 and S7). The test results show that SEIH can reliably maintain its intended functionality not only under minimal excitation but also under extreme mechanical stress, including harsh scenarios such as vehicle run-over tests.

This capability allows the SEIH system to be seamlessly integrated into smart-home environments for wireless control of smart devices, such as lighting systems (Figures 6E and S53; Video S8) and door access systems (Figures 6F and S54; Video S9), thereby enabling concurrent transmission of both energy and information tailored for event-triggered applications. Moreover, the SEIH system can be readily adapted as a self-powered human-machine interaction device that offers rapid response and precise control comparable to commercial wireless keyboards in playing a computer game (*Flappy Bird*) (Figures 6G and S55; Video S10). Meanwhile, an integration of four SEIH units expanded the versatility of the HMI device, further demonstrating its robustness and agility in handling complex user inputs required by the interactive computer game *Subway Surfers* (Figures 6H–6J and S56; Video S11). As one of the promising applications of TENGs, self-powered sensing for status monitoring has made significant strides over the past decade. Compared with existing event-triggered sensing implementations, our system demonstrates substantial improvements in terms of transmission distance and robustness (Figure 6K; Table S4).[23,24,43,45,46,63–74] These improvements stem from the highly interdisciplinary design of the SEIH system, which encompasses an origami-inspired structure, carefully selected triboelectric materials, an integrated fabrication process, a dedicated energy-regulation strategy, and a seamless coupling with an ultra-low-power sensing and wireless communication circuit.

Due to its foldable structure and high flexibility, the SEIH system lends itself well to integration with wearable devices. As demonstrated in Figure 6L and Video S12, we embedded it in an arm bag, and tapping it generates sufficient energy to support ambient temperature and humidity sensing. The data can be received by a custom-developed mobile app synchronized with an IoT platform, offering valuable input for evaluating environmental conditions and informing decisions, such as whether the surroundings are suitable for physical activity. In real-world event-triggered applications, the cold-start time of a self-powered system is a critical performance indicator. Compared with previous designs (Figure 1H; Table S1), our SEIH system not only autonomously performs sensing and communication tasks but also achieves a remarkably cold-start response of approximately 0.01 s (Figure S57).

DISCUSSION

In summary, we developed a diamond-tessellated, origami-inspired triboelectric nanogenerator (DT-TENG), which serves as the foundation for an SEIH system that achieves fully self-powered, event-triggered sensing and wireless communication. Enabled by its origami-inspired structure, special surface treatment, and dedicated energy-regulation strategy, the DT-TENG produces a three-dimensional triboelectrification effect that substantially boosts energy generation, achieving a peak power density of 548.33 W/m^3 and addressing longstanding issues, including high internal impedance and poor adaptability to practical electronic loads. In particular, utilizing an optimized ERC, the DT-TENG can harvest an average energy of approximately 136.87 μJ from a single gentle hand tap, which is sufficient to power a range of low-power electronics. By seamlessly integrating the DT-TENG, the ERC, and a tailored low-power sensing circuit, the resulting SEIH system is compatible with

(D) Voltage profiles showing capacitor charging and BLE signals received by the three receivers following a single hand-tap activation of the DT-TENG. Each spike indicates a successfully received BLE advertisement packet.
(E–G) Illustrative applications of the SEIH system operating in a fully self-powered manner, including (E) lighting system control, (F) door access system control, and (G) computer gaming (*Flappy Bird*). See Figures S53–S55 for test details.
(H and I) Demonstration of using a 4-unit SEIH array in playing the game *Subway Surfers*. See Figure S56 for test details.
(J) Signal patterns generated by the SEIH units and detected at the receiver in response to distinct triggering actions.
(K) Benchmark comparison of existing self-powered wireless sensing systems in terms of development timeline and wireless communication range. TENG-based systems at the sensor level still require external power sources, while the proposed SEIH system achieves full energy autonomy at the system level, supporting sensing, data acquisition, and wireless transmission without any external power.
(L) Demonstration of a fully self-powered wearable electronic using the SEIH unit for wireless temperature and humidity monitoring, with real-time IoT cloud synchronization and smartphone display.

commercial sensors for event-triggered monitoring. With a cold-start time as short as 10 ms, the SEIH system offers exceptional responsiveness, aligning well with the requirements of wearable electronics and IoT platforms that prioritize fast, autonomous, and low-power sensing. Through its event-driven architecture, the SEIH system exhibits broad applicability across various scenarios, ranging from motion detection and smart lighting to door access control, as well as human-machine interaction contexts, such as computer gaming and wearable sensing. By utilizing cost-effective fabrication techniques, specifically flexible printed circuit (FPC) technology and plasma surface treatment, the SEIH system achieves an optimal balance between scalability and output performance. These features position it as a promising solution for next-generation wearable electronics and large-scale IoT deployments.

METHODS

Device fabrication

The fabrication of the DT-TENG involves a four-step process to prepare a foldable structure and to correctly assemble the TENG elements. First, a flexible printed circuit board (FPCB) technique is utilized to fabricate and pattern electrode materials (copper) on a flexible substrate (Kapton). Next, a laser cutter is employed to apply dashed-line cuts along a predefined crease pattern on the FPCB. In the third step, selected electrodes are coated with dielectric films (FEP) that serve as both contact triboelectrification and dielectric layers. Finally, wires are soldered to the copper electrodes, and the TENG is folded along the customized crease pattern. The mechanical properties of the FEP and FPC films can be found in Tables S5 and S6.

Simulation

FE simulations were conducted using the commercial software COMSOL Multiphysics, while the development and folding processes were simulated in Rhino using the Grasshopper plugin.

Characterization and measurement

An electrometer (Keithley 6517) and a data acquisition card (NI 9102) were used to measure the electrical output of the DT-TENG and the SEIH system, with real-time waveforms displayed on an oscilloscope (RIGOL DHO1104 or Analog Discovery 2). The mechanical response of the DT-TENG was characterized using a custom-developed testbench consisting of the above measurement instruments, a linear motor (Kollmorgen), and a laser Doppler vibrometer (SOPTOP LV-S01). A universal testing machine (Instron 34TM-30) was used to characterize the compressive displacement behavior of the DT-TENG.

A plasma cleaner (ZEPTOW6, Diener) was employed to treat the surface of the FEP dielectric layer. The surface morphology and wear characteristics of the dielectric layer were analyzed using a white light interferometer (NPFLEX-1000).

The experiments conducted under controlled temperature and humidity conditions were performed using an environmental simulation chamber (KWNT-NX30), capable of simulating temperatures from 18°C to 30°C and relative humidity levels from 30% to 70% (see equipment in Figure S58).

A BLE sniffer (NRF52840 Dongle) was used to capture the BLE advertisement packets transmitted by the SEIH system. The collected data were then analyzed using Wireshark or TShark, in conjunction with Python scripts for Media Access Control (MAC) address filtering and parsing of specific Bluetooth packets.

The temperature and humidity data collected by the SEIH system were uploaded to an IoT platform supported by Arduino Cloud, enabling real-time remote monitoring and data visualization.

The effective area of the configurations shown in Figure 2H is calculated using the formula $\frac{S-S_0}{S} \times 100\%$, where S denotes the area contained by the outer contour of the configuration, and S_0 is the area of the geometric hollow inside the configuration (the white area inside the origami configuration in Figure 2H).

The peak power density of the DT-TENG is calculated using the formula P/V, where P is the peak power output, and V is the volume of the DT-TENG. In Figure 4H, the DT-TENG achieves a peak power of 9.87 mW. For the case where $n = 5$, the volume of the DT-TENG is 18,000 mm^3 (60 mm × 60 mm × 5 mm). Therefore, the resulting peak power density is approximately 548.33 W/m^3.

RESOURCE AVAILABILITY

Lead contact

Requests for further information and resources should be directed to and will be fulfilled by the lead contact, Guobiao Hu (guobiaohu@hkust-gz.edu.cn).

Materials availability

This study did not generate new, unique reagents.

Data and code availability

The data and code that support the conclusions of this study are available from the lead contact upon reasonable request.

ACKNOWLEDGMENTS

This work was supported by the National Natural Science Foundation of China (grant no. 52305135), the Guangdong Provincial Project (grant no. 2023QN10L545), the Guangzhou Municipal Science and Technology Project (grant no. 2023A03J0011), the Guangdong Provincial Key Lab of Integrated Communication, Sensing, and Computation for Ubiquitous Internet of Things (grant no. 2023B1212010007), and the Guangzhou Municipal Key Laboratory on Future Networked Systems (grant no. 2024A03J0623).

The authors gratefully acknowledge Mr. Xiang Gao and Mr. Tao Wang for their assistance with the circuit design and Mr. Rensheng Deng and Ms. Zhaorong Wan for their support in material characterization. Special thanks are extended to Mr. Ye Zhang, Mr. Chengyun Du, and Mr. Shuai Jiang for their help in the demonstration phase. The authors also thank Mr. Hengxu Du, Mr. Ziyue Xi, and Mr. Hongyong Yu for their contributions in the early stage of the experiments. Additional appreciation is given to Ms. Jingyi Liu for her assistance with figure illustrations.

The authors further acknowledge the Precision Measurement and Electrical Workshop, Materials, Design, and Manufacturing Facility (GZ), Materials Preparation Workshop, Materials Characterization and Preparation Facility, and Sustainable Atmospheric Environment Research Facility at the Hong Kong University of Science and Technology (Guangzhou) for their technical support.

AUTHOR CONTRIBUTIONS

G.H. conceived the idea and secured the funding. Y. Wang designed the experiments, conducted the tests, collected the data, prepared the figures,

Please cite this article in press as: Wang et al., Origami-structured triboelectric nanogenerator for energy and information co-harvesting from a single hand tap, Joule (2026), https://doi.org/10.1016/j.joule.2026.102338

and drafted the original manuscript. Y.L. and Y.Z. supported the experiments and figure preparation. Y. Wang and Y. Wu derived the theoretical formulations. Y. Wang also designed and developed the circuit boards. H.T. assisted in the circuit design. G.H., M.X., and Q.S. revised and polished the manuscript. G.H. supervised and guided the overall project.

DECLARATION OF INTERESTS

The authors declare no conflicts of interest.

SUPPLEMENTAL INFORMATION

Supplemental information can be found online at https://doi.org/10.1016/j.joule.2026.102338.

Received: August 4, 2025
Revised: October 14, 2025
Accepted: January 18, 2026

REFERENCES

1. Chen, J., and Wang, Z.L. (2017). Reviving Vibration Energy Harvesting and Self-Powered Sensing by a Triboelectric Nanogenerator. Joule *1*, 480–521. https://doi.org/10.1016/j.joule.2017.09.004.
2. Yang, Z., Zhou, S., Zu, J., and Inman, D. (2018). High-Performance Piezoelectric Energy Harvesters and Their Applications. Joule *2*, 642–697. https://doi.org/10.1016/j.joule.2018.03.011.
3. Zhang, Y., Rytkin, E., Zeng, L., Kim, J.U., Tang, L., Zhang, H., Mikhailov, A., Zhao, K., Wang, Y., Ding, L., et al. (2025). Millimetre-scale bioresorbable optoelectronic systems for electrotherapy. Nature *640*, 77–86. https://doi.org/10.1038/s41586-025-08726-4.
4. Zhang, C., He, L., Zhou, L., Yang, O., Yuan, W., Wei, X., Liu, Y., Lu, L., Wang, J., and Wang, Z.L. (2021). Active resonance triboelectric nanogenerator for harvesting omnidirectional water-wave energy. Joule *5*, 1613–1623. https://doi.org/10.1016/j.joule.2021.04.016.
5. Wang, J., Yurchenko, D., Hu, G., Zhao, L., Tang, L., and Yang, Y. (2021). Perspectives in flow-induced vibration energy harvesting. Appl. Phys. Lett. *119*, 100502. https://doi.org/10.1063/5.0063488.
6. Li, Y., Wang, Y., Li, Y., Peng, X., Li, D., Xia, X., Li, X., Zi, Y., and Hu, G. (2025). Heat-powered IoT node: A synergistic fusion of thermoacoustic engine and triboelectric nanogenerator. Appl. Phys. Lett. *126*, 023902. https://doi.org/10.1063/5.0244410.
7. Zhao, T., Li, Z., Niu, B., Xie, G., Shangguan, L., Zhang, M., Zhu, Y., Ma, Y., Hu, C., and Li, Y. (2025). A pendulum-based nanogenerator for high-entropy wave energy harvesting. Nat. Commun. *16*, 5480. https://doi.org/10.1038/s41467-025-60443-8.
8. Zhao, T., Niu, B., Xie, G., Hu, C., Liu, B., Xu, M., and Ma, Y. (2022). A High Output Triboelectric–Electromagnetic Hybrid Generator Based on In-Phase Parallel Connection. Adv. Mater. Technol. *7*, 2101485. https://doi.org/10.1002/admt.202101485.
9. Fan, F.-R., Tian, Z.-Q., and Lin Wang, Z. (2012). Flexible triboelectric generator. Nano Energy *1*, 328–334. https://doi.org/10.1016/j.nanoen.2012.01.004.
10. Zou, H., Guo, L., Xue, H., Zhang, Y., Shen, X., Liu, X., Wang, P., He, X., Dai, G., Jiang, P., et al. (2020). Quantifying and understanding the triboelectric series of inorganic non-metallic materials. Nat. Commun. *11*, 2093. https://doi.org/10.1038/s41467-020-15926-1.
11. Cheng, T., Shao, J., and Wang, Z.L. (2023). Triboelectric nanogenerators. Nat. Rev. Methods Primers *3*, 39. https://doi.org/10.1038/s43586-023-00220-3.
12. Choi, D., Lee, Y., Lin, Z.-H., Cho, S., Kim, M., Ao, C.K., Soh, S., Sohn, C., Jeong, C.K., Lee, J., et al. (2023). Recent Advances in Triboelectric Nanogenerators: From Technological Progress to Commercial Applications. ACS Nano *17*, 11087–11219. https://doi.org/10.1021/acsnano.2c12458.
13. Wang, Y., Liu, X., Wang, Y., Wang, H., Wang, H., Zhang, S.L., Zhao, T., Xu, M., and Wang, Z.L. (2021). Flexible Seaweed-Like Triboelectric Nanogenerator as a Wave Energy Harvester Powering Marine Internet of Things. ACS Nano *15*, 15700–15709. https://doi.org/10.1021/acsnano.1c05127.
14. Zhao, C., Du, T., Ge, B., Xi, Z., Qian, Z., Wang, Y., Wang, J., Dong, F., Shen, D., Zhan, Z., et al. (2024). Coaxial Flexible Fiber-Shaped Triboelectric Nanogenerator Assisted by Deep Learning for Self-Powered Vibration Monitoring. Small *20*, e2307680. https://doi.org/10.1002/smll.202307680.
15. Zhao, C., Liu, D., Wang, Y., Hu, Z., Zhang, Q., Zhang, Z., Wang, H., Du, T., Zou, Y., Yuan, H., et al. (2022). Highly-stretchable rope-like triboelectric nanogenerator for self-powered monitoring in marine structures. Nano Energy *94*, 106926. https://doi.org/10.1016/j.nanoen.2022.106926.
16. Yu, H., Xi, Z., Du, H., Yang, H., Qian, Z., Guo, X., Guo, Y., Huang, Y., Du, T., and Xu, M. (2024). High Performance and Stackable Trampoline Like-Triboelectric Vibration Energy Harvester for In-Situ Powering Sensor Node with Data Wirelessly Transmitted Over 1000-m. Adv. Energy Mater. *14*, 2400585. https://doi.org/10.1002/aenm.202400585.
17. Xi, Z., Du, H., Wang, Y., Yu, H., Dai, S., Fan, M., Liu, J., Su, Q., Wang, H., Hu, G., et al. (2025). A ternary-dielectric rolling TENG array for robust ocean energy harvesting and distributed environmental monitoring. Nano Energy *143*, 111318. https://doi.org/10.1016/j.nanoen.2025.111318.
18. Wang, Y., Du, H., Yang, H., Xi, Z., Zhao, C., Qian, Z., Chuai, X., Peng, X., Yu, H., Zhang, Y., et al. (2024). A rolling-mode triboelectric nanogenerator with multi-tunnel grating electrodes and opposite-charge-enhancement for wave energy harvesting. Nat. Commun. *15*, 6834. https://doi.org/10.1038/s41467-024-51245-5.
19. Wu, H., Wang, S., Wang, Z., and Zi, Y. (2021). Achieving ultrahigh instantaneous power density of 10 MW/m2 by leveraging the opposite-charge-enhanced transistor-like triboelectric nanogenerator (OCT-TENG). Nat. Commun. *12*, 5470. https://doi.org/10.1038/s41467-021-25753-7.
20. Xia, X., Zhou, Z., Shang, Y., Yang, Y., and Zi, Y. (2023). Metallic glass-based triboelectric nanogenerators. Nat. Commun. *14*, 1023. https://doi.org/10.1038/s41467-023-36675-x.
21. He, S., Dai, J., Wan, D., Sun, S., Yang, X., Xia, X., and Zi, Y. (2024). Biomimetic bimodal haptic perception using triboelectric effect. Sci. Adv. *10*, eado6793. https://doi.org/10.1126/sciadv.ado6793.
22. Zhao, C., Wang, Z., Wang, Y., Qian, Z., Tan, Z., Chen, Q., Pan, X., Xu, M., and Lai, Y.C. (2023). MXene-Composite-Enabled Ultra-long-Distance Detection and Highly Sensitive Self-Powered Noncontact Triboelectric Sensors and Their Applications in Intelligent Vehicle Perception. Adv. Funct. Mater. *33*, 2306381. https://doi.org/10.1002/adfm.202306381.
23. Li, M., Lu, H.-W., Wang, S.-W., Li, R.-P., Chen, J.-Y., Chuang, W.-S., Yang, F.-S., Lin, Y.-F., Chen, C.-Y., and Lai, Y.-C. (2022). Filling the gap between topological insulator nanomaterials and triboelectric nanogenerators. Nat. Commun. *13*, 938. https://doi.org/10.1038/s41467-022-28575-3.
24. Shao, B., Lu, M.-H., Wu, T.-C., Peng, W.-C., Ko, T.-Y., Hsiao, Y.-C., Chen, J.-Y., Sun, B., Liu, R., and Lai, Y.-C. (2024). Large-area, untethered, metamorphic, and omnidirectionally stretchable multiplexing self-powered triboelectric skins. Nat. Commun. *15*, 1238. https://doi.org/10.1038/s41467-024-45611-6.
25. Cheng, G.-G., Jiang, S.-Y., Li, K., Zhang, Z.-Q., Wang, Y., Yuan, N.-Y., Ding, J.-N., and Zhang, W. (2017). Effect of argon plasma treatment on the output performance of triboelectric nanogenerator. Appl. Surf. Sci. *412*, 350–356. https://doi.org/10.1016/j.apsusc.2017.03.255.
26. Zhang, X.-S., Han, M.-D., Wang, R.-X., Meng, B., Zhu, F.-Y., Sun, X.-M., Hu, W., Wang, W., Li, Z.-H., and Zhang, H.-X. (2014). High-performance triboelectric nanogenerator with enhanced energy density based on single-step fluorocarbon plasma treatment. Nano Energy *4*, 123–131. https://doi.org/10.1016/j.nanoen.2013.12.016.

Please cite this article in press as: Wang et al., Origami-structured triboelectric nanogenerator for energy and information co-harvesting from a single hand tap, Joule (2026), https://doi.org/10.1016/j.joule.2026.102338

27. Cheng, X., Meng, B., Chen, X., Han, M., Chen, H., Su, Z., Shi, M., and Zhang, H. (2016). Single-Step Fluorocarbon Plasma Treatment-Induced Wrinkle Structure for High-Performance Triboelectric Nanogenerator. Small *12*, 229–236. https://doi.org/10.1002/smll.201502720.

28. Luo, J., and Wang, Z.L. (2020). Recent progress of triboelectric nanogenerators: From fundamental theory to practical applications. EcoMat *2*, e12059. https://doi.org/10.1002/eom2.12059.

29. Fu, H., Mei, X., Yurchenko, D., Zhou, S., Theodossiades, S., Nakano, K., and Yeatman, E.M. (2021). Rotational energy harvesting for self-powered sensing. Joule *5*, 1074–1118. https://doi.org/10.1016/j.joule.2021.03.006.

30. Zhang, C., Hao, Y., Lu, X., Su, W., Zhang, H., Wang, Z.L., and Li, X. (2025). Advances in TENGs for Marine Energy Harvesting and In Situ Electrochemistry. Nano-Micro Lett. *17*, 124. https://doi.org/10.1007/s40820-024-01640-w.

31. Pang, Y., Cao, Y., Derakhshani, M., Fang, Y., Wang, Z.L., and Cao, C. (2021). Hybrid Energy-Harvesting Systems Based on Triboelectric Nanogenerators. Matter *4*, 116–143. https://doi.org/10.1016/j.matt.2020.10.018.

32. Pathak, M., and Kumar, R. (2021). Synchronous Inductor Switched Energy Extraction Circuits for Triboelectric Nanogenerator. IEEE Access *9*, 76938–76954. https://doi.org/10.1109/ACCESS.2021.3082499.

33. Wang, Z., Tang, Q., Shan, C., Du, Y., He, W., Fu, S., Li, G., Liu, A., Liu, W., and Hu, C. (2021). Giant performance improvement of triboelectric nanogenerator systems achieved by matched inductor design. Energy Environ. Sci. *14*, 6627–6637. https://doi.org/10.1039/D1EE02852A.

34. Niu, S., Liu, Y., Zhou, Y.S., Wang, S., Lin, L., and Wang, Z.L. (2015). Optimization of Triboelectric Nanogenerator Charging Systems for Efficient Energy Harvesting and Storage. IEEE Trans. Electron Devices *62*, 641–647. https://doi.org/10.1109/TED.2014.2377728.

35. Hu, T., Wang, H., Harmon, W., Bamgboje, D., and Wang, Z.-L. (2022). Current Progress on Power Management Systems for Triboelectric Nanogenerators. IEEE Trans. Power Electron. *37*, 9850–9864. https://doi.org/10.1109/TPEL.2022.3156871.

36. Liu, W., Wang, Z., Wang, G., Zeng, Q., He, W., Liu, L., Wang, X., Xi, Y., Guo, H., Hu, C., et al. (2020). Switched-capacitor-convertors based on fractal design for output power management of triboelectric nanogenerator. Nat. Commun. *11*, 1883. https://doi.org/10.1038/s41467-020-15373-y.

37. Niu, S., Wang, X., Yi, F., Zhou, Y.S., and Wang, Z.L. (2015). A universal self-charging system driven by random biomechanical energy for sustainable operation of mobile electronics. Nat. Commun. *6*, 8975. https://doi.org/10.1038/ncomms9975.

38. Fu, X., Jiang, Z., Cao, J., Dong, Z., Liu, G., Zhu, M., and Zhang, C. (2024). A near-zero quiescent power breeze wake-up anemometer based on a rolling-bearing triboelectric nanogenerator. Microsyst. Nanoeng. *10*, 51. https://doi.org/10.1038/s41378-024-00676-7.

39. Fu, X., Xu, S., Gao, Y., Zhang, X., Liu, G., Zhou, H., Lv, Y., Zhang, C., and Wang, Z.L. (2021). Breeze-Wind-Energy-Powered Autonomous Wireless Anemometer Based on Rolling Contact-Electrification. ACS Energy Lett. *6*, 2343–2350. https://doi.org/10.1021/acsenergylett.1c00704.

40. Liu, Z., Hu, Y., Qu, X., Liu, Y., Cheng, S., Zhang, Z., Shan, Y., Luo, R., Weng, S., Li, H., et al. (2024). A self-powered intracardiac pacemaker in swine model. Nat. Commun. *15*, 507. https://doi.org/10.1038/s41467-023-44510-6.

41. Hinchet, R., Yoon, H.-J., Ryu, H., Kim, M.-K., Choi, E.-K., Kim, D.-S., and Kim, S.-W. (2019). Transcutaneous ultrasound energy harvesting using capacitive triboelectric technology. Science *365*, 491–494. https://doi.org/10.1126/science.aan3997.

42. Chung, Y., Jeong, J.-M., Hwang, J.-H., Kim, Y.-J., Park, B.-J., Cho, D.S., Cho, Y., Suh, S.-J., Choi, B.-O., Park, H., et al. (2024). Gigantic triboelectric power generation overcoming acoustic energy barrier using metal-liquid coupling. Joule *8*, 2681–2695. https://doi.org/10.1016/j.joule.2024.06.016.

43. Wang, H., Wang, J., Yao, K., Fu, J., Xia, X., Zhang, R., Li, J., Xu, G., Wang, L., Yang, J., et al. (2021). A paradigm shift fully self-powered long-distance wireless sensing solution enabled by discharge-induced displacement current. Sci. Adv. *7*, eabi6751. https://doi.org/10.1126/sciadv.abi6751.

44. Mallineni, S.S.K., Dong, Y., Behlow, H., Rao, A.M., and Podila, R. (2018). A Wireless Triboelectric Nanogenerator. Adv. Energy Mater. *8*, 1702736. https://doi.org/10.1002/aenm.201702736.

45. Zhang, C., Chen, J., Xuan, W., Huang, S., You, B., Li, W., Sun, L., Jin, H., Wang, X., Dong, S., et al. (2020). Conjunction of triboelectric nanogenerator with induction coils as wireless power sources and self-powered wireless sensors. Nat. Commun. *11*, 58. https://doi.org/10.1038/s41467-019-13653-w.

46. Wen, F., Wang, H., He, T., Shi, Q., Sun, Z., Zhu, M., Zhang, Z., Cao, Z., Dai, Y., Zhang, T., et al. (2020). Battery-free short-range self-powered wireless sensor network (SS-WSN) using TENG based direct sensory transmission (TDST) mechanism. Nano Energy *67*, 104266. https://doi.org/10.1016/j.nanoen.2019.104266.

47. Yu, Y., Li, H., Zhang, X., Gao, Q., Yang, B., Wang, Z.L., and Cheng, T. (2024). Substantially boosting performance of triboelectric nanogenerators via a triboelectrification enhancement effect. Joule *8*, 1855–1868. https://doi.org/10.1016/j.joule.2024.04.013.

48. Wang, H., Xu, L., Bai, Y., and Wang, Z.L. (2020). Pumping up the charge density of a triboelectric nanogenerator by charge-shuttling. Nat. Commun. *11*, 4203. https://doi.org/10.1038/s41467-020-17891-1.

49. Pu, X., Liu, M., Chen, X., Sun, J., Du, C., Zhang, Y., Zhai, J., Hu, W., and Wang, Z.L. (2017). Ultrastretchable, transparent triboelectric nanogenerator as electronic skin for biomechanical energy harvesting and tactile sensing. Sci. Adv. *3*, e1700015. https://doi.org/10.1126/sciadv.1700015.

50. Su, E., Xu, S., Wang, Z., Xu, Z., Pan, S., Wang, Z.L., and Cao, L.N.Y. (2025). Buoyancy-gravity optimized triboelectric nanogenerators via conductive 3D printing for robust wave energy harvesting. Mater. Sci. Eng.: R: Rep. *164*, 100953. https://doi.org/10.1016/j.mser.2025.100953.

51. Cao, L.N.Y., Su, E., Xu, Z., and Wang, Z.L. (2023). Fully enclosed microbeads structured TENG arrays for omnidirectional wind energy harvesting with a portable galloping oscillator. Mater. Today *71*, 9–21. https://doi.org/10.1016/j.mattod.2023.11.001.

52. Qiu, H., Wang, H., Xu, L., Zheng, M., and Wang, Z.L. (2023). Brownian motor inspired monodirectional continuous spinning triboelectric nanogenerators for extracting energy from irregular gentle water waves. Energy Environ. Sci. *16*, 473–483. https://doi.org/10.1039/D2EE03395J.

53. Hu, G., Zhao, C., Yang, Y., Li, X., and Liang, J. (2022). Triboelectric energy harvesting using an origami-inspired structure. Appl. Energy *306*, 118037. https://doi.org/10.1016/j.apenergy.2021.118037.

54. Jiang, Y., Chen, P., Han, J., Liang, X., Ming, Y., Liu, S., Jiang, T., and Wang, Z.L. (2025). High-performance triboelectric nanogenerator based on a double-spiral zigzag-origami structure for continuous sensing and signal transmission in marine environment. Interdiscip. Mater. *4*, 201–212. https://doi.org/10.1002/idm2.12226.

55. Chen, Y., Peng, R., and You, Z. (2015). Applied origami. Origami of thick panels. Science *349*, 396–400. https://doi.org/10.1126/science.aab2870.

56. Chen, Y., Feng, H., Ma, J., Peng, R., and You, Z. (2016). Symmetric waterbomb origamiSoc. Proc. Math. Phys. Eng. Sci. *472*, 20150846. https://doi.org/10.1098/rspa.2015.0846

57. Zhu, Y., Schenk, M., and Filipov, E.T. (2022). A Review on Origami Simulations: From Kinematics, To Mechanics, Toward Multiphysics. Appl. Mech. Rev. *74*. https://doi.org/10.1115/1.4055031.

58. Han, H., Tang, L., Cao, D., and Liu, L. (2020). Modeling and analysis of dynamic characteristics of multi-stable waterbomb origami base. Nonlinear Dyn. *102*, 2339–2362. https://doi.org/10.1007/s11071-020-06082-8.

59. Suh, J.-E., Miyazawa, Y., Yang, J., and Han, J.-H. (2022). Self-Reconfiguring and Stiffening Origami Tube. Adv. Eng. Mater. *24*, 2101202. https://doi.org/10.1002/adem.202101202.

Please cite this article in press as: Wang et al., Origami-structured triboelectric nanogenerator for energy and information co-harvesting from a single hand tap, Joule (2026), https://doi.org/10.1016/j.joule.2026.102338

60. Niu, S., Wang, S., Lin, L., Liu, Y., Zhou, Y.S., Hu, Y., and Wang, Z.L. (2013). Theoretical study of contact-mode triboelectric nanogenerators as an effective power source. Energy Environ. Sci. *6*, 3576. https://doi.org/10.1039/c3ee42571a.

61. Niu, S., and Wang, Z.L. (2015). Theoretical systems of triboelectric nanogenerators. Nano Energy *14*, 161–192. https://doi.org/10.1016/j.nanoen.2014.11.034.

62. Wang, Y., Qian, Z., Zhao, C., Wang, Y., Jiang, K., Wang, J., Meng, Z., Li, F., Zhu, C., Chen, P., et al. (2023). Highly Adaptive Triboelectric-Electromagnetic Hybrid Nanogenerator for Scavenging Flow Energy and Self-Powered Marine Wireless Sensing. Adv. Mater. Technol. *8*, 2201245. https://doi.org/10.1002/admt.202201245.

63. Zhu, G., Yang, W.Q., Zhang, T., Jing, Q., Chen, J., Zhou, Y.S., Bai, P., and Wang, Z.L. (2014). Self-Powered, Ultrasensitive, Flexible Tactile Sensors Based on Contact Electrification. Nano Lett. *14*, 3208–3213. https://doi.org/10.1021/nl5005652.

64. Jing, Q., Xie, Y., Zhu, G., Han, R.P.S., and Wang, Z.L. (2015). Self-powered thin-film motion vector sensor. Nat. Commun. *6*, 8031. https://doi.org/10.1038/ncomms9031.

65. Chen, J., Zhu, G., Yang, J., Jing, Q., Bai, P., Yang, W., Qi, X., Su, Y., and Wang, Z.L. (2015). Personalized Keystroke Dynamics for Self-Powered Human–Machine Interfacing. ACS Nano *9*, 105–116. https://doi.org/10.1021/nn506832w.

66. Li, S., Peng, W., Wang, J., Lin, L., Zi, Y., Zhang, G., and Wang, Z.L. (2016). All-Elastomer-Based Triboelectric Nanogenerator as a Keyboard Cover To Harvest Typing Energy. ACS Nano *10*, 7973–7981. https://doi.org/10.1021/acsnano.6b03926.

67. Luo, J., Wang, Z., Xu, L., Wang, A.C., Han, K., Jiang, T., Lai, Q., Bai, Y., Tang, W., Fan, F.R., et al. (2019). Flexible and durable wood-based triboelectric nanogenerators for self-powered sensing in athletic big data analytics. Nat. Commun. *10*, 5147. https://doi.org/10.1038/s41467-019-13166-6.

68. Kuang, H., Huang, S., Zhang, C., Chen, J., Shi, L., Zeng, X., Li, Y., Yang, Z., Wang, X., Dong, S., et al. (2022). Electric-Field-Resonance-Based Wireless Triboelectric Nanogenerators and Sensors. ACS Appl. Mater. Interfaces *14*, 794–804. https://doi.org/10.1021/acsami.1c19075.

69. Zhao, H., Xu, M., Shu, M., An, J., Ding, W., Liu, X., Wang, S., Zhao, C., Yu, H., Wang, H., et al. (2022). Underwater wireless communication via TENG-generated Maxwell's displacement current. Nat. Commun. *13*, 3325. https://doi.org/10.1038/s41467-022-31042-8.

70. Zu, L., Wen, J., Wang, S., Zhang, M., Sun, W., Chen, B., and Wang, Z.L. (2023). Multiangle, self-powered sensor array for monitoring head impacts. Sci. Adv. *9*, eadg5152. https://doi.org/10.1126/sciadv.adg5152.

71. Wang, T., Wang, C., Zeng, Q., Gu, G., Wang, X., Cheng, G., and Du, Z. (2024). A real-time, self-powered wireless pressure sensing system with efficient coupling energy harvester, sensing, and communication modules. Nano Energy *125*, 109533. https://doi.org/10.1016/j.nanoen.2024.109533.

72. Chen, M., Ji, M., Huang, L., Wu, N., Jiang, T., Li, C., Li, W., Yu, B., Luo, J., Li, X., et al. (2025). Highly elastic, lightweight, and high-performance all-aerogel triboelectric nanogenerator for self-powered intelligent fencing training. Mater. Sci. Eng.: R: Rep. *165*, 101004. https://doi.org/10.1016/j.mser.2025.101004.

73. Hong, H., Yan, C., Hu, Y., Yang, J., Chen, B., Liu, L., Wang, Z., and Wu, H. (2025). Achieving Ultra-High-Power Output in Triboelectric Energy Harvesters by Torrent-Like Charge Regulation. Adv. Mater. *37*, e2506136. https://doi.org/10.1002/adma.202506136.

74. Ji, P., Wen, J., Gao, X., Li, H., Cai, H., Lv, K., Wang, Z.L., and Chen, B. (2025). Roadbed tribological energy harvester. Sci. Adv. *11*, eadv9379. https://doi.org/10.1126/sciadv.adv9379.